

Acoustic Emission and Digital Image Correlation as Complementary Techniques for Laboratory and Field Research

Rami Carmi, P.A. Vanniamparambil, J. Cuadra, K. Hazeli, S. Rajaram, U. Guclu, Arrie Bussiba, I. Bartoli, and Antonios Kotsos

Abstract This article presents the advantages of combining Acoustic Emission (AE) and Digital Image Correlation (DIC) in nondestructive testing (NDT) applications focusing on in situ damage monitoring. This data-fusion approach is used herein to characterize the mechanical and damage behavior of a fiber metal laminate (Glare 1A) tested in both tension and fatigue. Furthermore, the approach is used to investigate the structural behavior of partially grouted reinforced masonry walls. The obtained AE datasets were post-processed, in combination with DIC and mechanical information, using signal processing and pattern recognition techniques to investigate progressive failure of the Glare 1A. In the case of the masonry wall specimens, DIC clearly identified critical damage areas as a function of applied loading, while AE was capable to monitor the damage process and reveal changes in the overall behavior. The presented analysis demonstrates the potential of integrating AE and DIC in data-driven damage mechanics investigations at multiple time and length scales.

1 Introduction

Acoustic Emission (AE) and Digital Image Correlation (DIC) are two Nondestructive Testing (NDT) techniques that are rarely used simultaneously, although the combined information has shown that it can greatly assist material characterization

R. Carmi • A. Bussiba
NRCN-Negev, P.O.B. 9001, Beer Sheva 84190, Israel
e-mail: carmo_nm@netvision.net.il

P.A. Vanniamparambil • J. Cuadra • K. Hazeli • S. Rajaram • U. Guclu
I. Bartoli • A. Kotsos (✉)
Drexel University, Philadelphia, PA 19104, USA
e-mail: prashanth288@gmail.com; AKotsos@coe.drexel.edu

from deformation, fracture, and damage evolution aspects, as demonstrated in this article.

AE can be used to monitor an entire component using a relatively small number of sensors capable to detect transient elastic waves generated due to sudden microstructural changes in the material [1]. In addition to real time extracted AE parameters with relevance to the deformation and damage process, postmortem analyses can be used to separate the signals into clusters that contain AE information from various failure mechanisms activated during loading.

The application of the DIC method can be achieved with one camera (for 2D) or two cameras (for 3D measurements) [2]. The method is based on tracking gray scale light intensity on the surface of the tested item as loading is applied, which is then used to compute tensorial components of in and out of plane strains. The final result is typically a full field strain map of the loaded structure developing with time [3–5]. This technique has the potential of visualizing defects or strain evolution on the surface with a very high accuracy ($\sim 100 \mu\epsilon$).

These NDT techniques have been considered by the authors as complementary ones and have been already applied for understanding fundamental plasticity as well as crack initiation and growth in light metal alloys, progressive damage development in fiber-reinforced polymer composites and failure of structural components used in civil engineering applications [6–8]. The fundamental reason for this integration is that AE can monitor the structure in terms of both volumetric and surface effects, though without the capability to visualize them, whereas DIC detects defects and provides full field strain maps, though only on the surface of the monitored specimen or component. Therefore the integration of these two NDT techniques by definition has the potential to lead to more quantitative and comprehensive results compared to the stand-alone use of each method as also demonstrated in this article.

The research work presented herein first illustrates the capabilities of the combined AE-DIC method in investigating the tensile and fatigue behavior of a fiber-reinforced metal laminate (FML). Specifically, Glare 1A (registered trademark of ALCOA) is a type of hybrid composite consisting of alternating thin layers of metal sheets and fiber-reinforced epoxy prepregs [9, 10]. This composite is used as shielding material against debris and meteors in space stations, and as aircraft skin [11]. Second, larger scale testing was conducted on partially grouted masonry wall specimens to examine their structural behavior for different types of reinforcement architectures.

The results of the research work in this paper are discussed with emphasis on the AE response by using relevant DIC information that focuses on providing a better and more quantitative understanding of the damage progress.

2 Materials, Structures, and Methods

2.1 FML Glare 1A

The characterized FML composite was Glare 1A with 1.4 mm in thickness. This material has a stacking sequence of three layers (each 0.3 mm in thickness) of Al-7475T76 alloy, and two prepreg (containing a mold-mat chemical thickening agent) layers of S2-glass fibers (each 0.25 mm in thickness) in an epoxy resin (designated FM-94 [10, 12]) with a 0.6 volume fraction of unidirectional fibers. At the final stage of processing, the FML was post-stretched by 0.4 % in order to achieve residual compressive stress in the metal and residual tensile stress in the fiber–resin interface. More details on the manufacturing process can be found elsewhere [9, 10]. A metallographic cross section of the composite with unidirectional fibers is illustrated in Fig. 1.

The mechanical behavior of flat Glare 1A specimens was characterized using both quasi-static and cyclic loading in a MTS computerized servo-hydraulic system with a load capacity of 100 KN. The commercially available Micro II AE system (manufactured by MISTRAS) was operated by using the AWin software and by mounting on the specimens' surface two resonant sensors (Pico) with 2/4/6 AST preamplifiers and band-pass filters between 20 kHz and 1 MHz. An amplitude threshold of 32 dB was selected in accordance with measured background noise levels. AE signals and post-processing data were analyzed using the NOESIS software (MISTRAS). Prior testing, both the sensors' sensitivity and material wave speeds were measured.

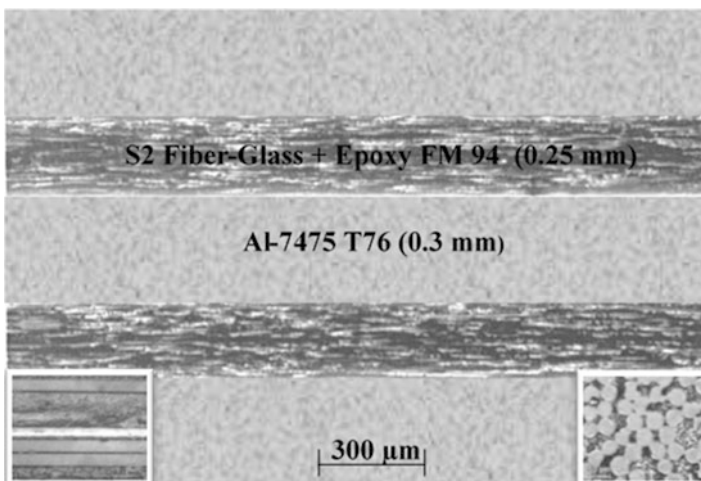


Fig. 1 The layup of Glare 1A containing unidirectional glass fibers in an epoxy matrix as well as aluminum alloy layers; longitudinal and perpendicular cross sections of the sample located in lower left and right images, respectively. Fiber diameter was 10 μm

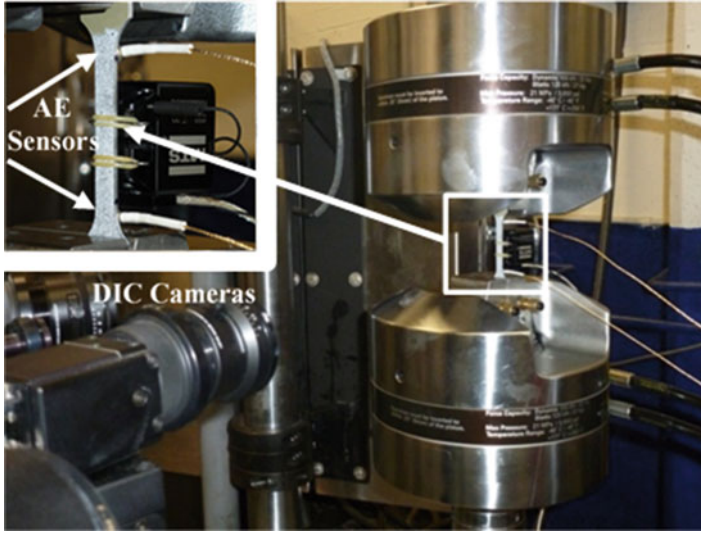


Fig. 2 Experimental setup focusing on the speckle painted specimen and the location of the AE sensors and the extensometer

A 5 megapixel GOM 3D DIC system (distributed by Trilion Quality Systems) was used in parallel to the AE system to acquire DIC data. The cameras were calibrated for a field of view (FOV) of 55×44 mm and were positioned 40 cm away from the specimen to capture the required FOV. A random speckle pattern (black dots on white paint) was applied on the specimen surface to track the deformation process with a strain sensitivity of about $60 \mu\epsilon$. For the monotonic tests, the images were recorded at a rate of 1 Hz, while in the fatigue tests a rate of 22 Hz was used.

For quantitative understanding of the mechanical behavior of the FML, a comprehensive study was conducted on its constituents, namely, S2-glass fibers, Al-alloy, epoxy resin, and interface matrix/fibers. To this aim, besides the flat Glare specimens used for the uniaxial tensile and fatigue tests, special specimens were designed for fiber and matrix/fiber characterization. Furthermore, and although DIC was used, an extensometer (manufactured by MTS) with a gauge length of 10 mm was additionally used. A constant displacement rate of 0.5 mm/min was selected for the quasi-static tests, while a sinusoidal wave loading profile with frequency equal to 5 Hz and a load ratio of 0.1 was used for the fatigue tests with different maximum stresses related to the measured yield stress. Metallographic and fractographic studies were also performed in order to track micro-cracking, delamination, other deformation and fracture features, as well as to assist the AE classification process.

Figure 2 illustrates the experimental setup that includes the combined AE and DIC systems. A closer view of the speckle painted specimen for DIC measurements, as well as the attached AE sensors and used extensometer is given in the upper left corner of Fig. 2.

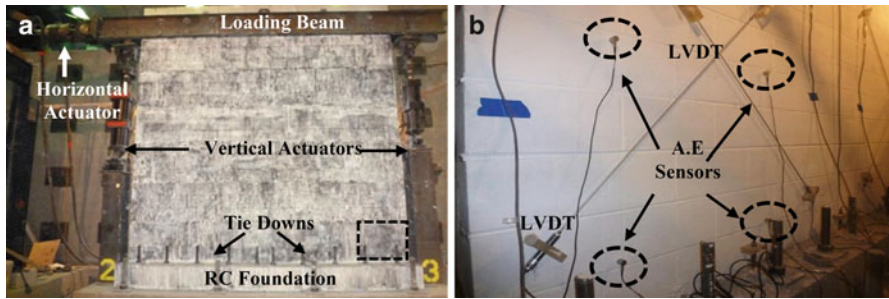


Fig. 3 Experimental setup of the tested masonry wall; (a) front view with coating for DIC measurements, (b) rear view showing the AE sensors and LVDTs for displacement measurements

2.2 Partially Grouted Reinforced Masonry Walls

The tested structure consisted of partially grouted masonry wall specimens reinforced with steel beams in different configurations for comparison of their response. The wall was base-fastened and loaded by a hydraulic actuator mounted (Fig. 3a) in the upper left corner of the wall in displacement control using a triangle wave at a frequency of 0.02 Hz. The wave amplitude was increased every two cycles until significant damage or final fracture was observed. The damage evolution was monitored simultaneously by DIC, AE, several LVDTs and was assisted by visual inspections. For the DIC measurements, a FOV of approximately $3,700 \times 4,000$ mm was used with the cameras positioned 6 m from the wall. The distance between the two lenses was 1.92 m. A random speckle pattern was created on the surface using spray paint and perforated sheets. The sampling rate was 1–2 frames per second depending on the overall duration of each test. The noise level for strain measurement was measured $50 \mu\text{m/m}$. For AE measurements, four resonant R15 sensors (MISTRAS) were mounted on the back side of the wall near the lower right corner using hot-glue (Fig. 3b). In order to obtain appropriate signals for representative source localization, a square configuration with AE sensors placed 1 m apart was selected. The same AE system and software were used; a threshold of 44 dB was chosen. Pretests of 0.3 mm pencil lead break (PLB) [13] were performed in order to determine values for appropriate AE parameters in the system.

3 Experimental Results

3.1 Glare 1A Constituent

Figure 4 illustrates the mechanical and acoustic responses of Al-Alloy specimens in terms of AE counts and cumulative AE energy. As shown, significant AE activity initiates near yielding at $\sim 1\%$ true strain. The sudden increase in AE activity was

Fig. 4 Mechanical and acoustic responses combined with DIC measurements of Al-7475 T76 specimens in quasi-static tensile tests

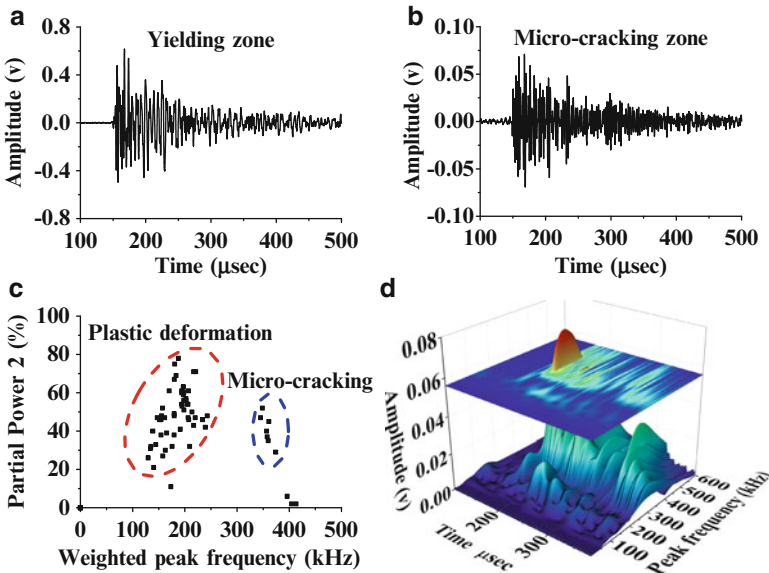
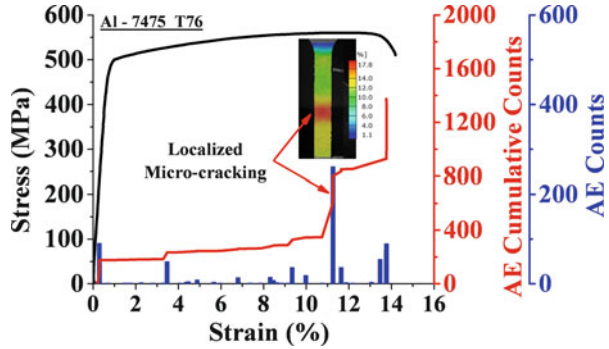


Fig. 5 AE results obtained by testing Al alloy samples: (a) representative AE waveform obtained near yielding, (b) waveform corresponding to micro-cracking, (c) weighted peak frequency versus partial power for several AE waveforms, (d) wavelet analysis of the waveform shown in (b) indicating a dominant peak frequency of 400 kHz

followed by a stage of moderate AE recordings up to ~11 % strain at which point DIC confirmed (see arrows) the onset of micro-cracking in the middle of the gauge area. This pronounced activity was followed by another stage of slow AE recordings until a final burst at the fracture point. The results in Fig. 4 clearly indicate dominant stages of plastic deformation and micro-cracking initiation/evolution. The existence of the aforementioned micro-mechanisms can be further seen by the different AE waveforms as depicted in Fig. 5a, b. The waveform in Fig. 5a was

Table 1 Frequency features and their definition

Feature	Definition
Peak frequency [kHz]	Maximum of frequency spectrum f_{peak}
Weighted peak frequency	$f_{\text{wpf}} = \sqrt{f_{\text{peak}} \cdot f_{\text{centroid}}}$
Frequency centroid	$f_{\text{centroid}} = \frac{\int f \cdot A(f) df}{\int A(f) df}$ $A(f) = \text{Amplitude at frequency } f$
Partial power [%]	Fraction of frequency spectrum
Partial power 1 [%]	0–150 kHz
Partial power 2 [%]	150–300 kHz
Partial power 3 [%]	300–450 kHz
Partial power 4 [%]	450–600 kHz

collected in the quasi-plateau region following the macroscopically observed yielding, while the waveform in Fig. 5b was recorded right at the transition point (~11 % strain).

A pattern recognition technique [14–16] was applied using the k-means algorithm. The classification procedure was based on the weighted peak frequency and is described elsewhere [17], and therefore it will not be repeated here. Table 1 summarizes the features which were used to classify the AE data.

AE data in Fig. 5c are displayed in terms of the weighted peak frequency (PF) and a partial power defined by FFT analysis. This two-dimensional feature projection reveals two dominant groups of AE signals, one in the 150–200 kHz range (plastic deformation) and the second between 350 and 400 kHz (micro-cracking). A representative wavelet analysis of the micro-cracking waveform in Fig. 5b is shown in Fig. 5d; a PF of around 400 kHz is clearly identified.

Results from a similar study performed on fiber bundle specimens are shown in Fig. 6. It should be emphasized based on the waveform of Fig. 6a that AE from a fiber breakage exhibits a rapid decay as compared to the more moderate decay shown in Fig. 5a for the Al-alloy specimen. Figure 6b, c show results from both frequency and time domain analysis; a dominant frequency of 450 kHz and AE amplitude between 50 and 90 dB (Fig. 6c) were found. Finally wavelet analysis shows in 3D display the measured PF of the fiber fracture.

To complete the constituent's characterization, matrix/fiber specimens were also tested and the results are shown in Fig. 7. For the waveform in Fig. 7a, three characteristic frequencies appeared in the wavelet analysis as shown in Fig. 7b. The 450 kHz one was already attributed to fiber breakage, while the other two of approximately 50 and 150 kHz are related to matrix and interface cracking, respectively. This conclusion is also based on AE waves recorded at early stages of loading (Fig. 7c) which have one characteristic frequency of ~100 kHz (Fig. 7d) associated with matrix cracking.

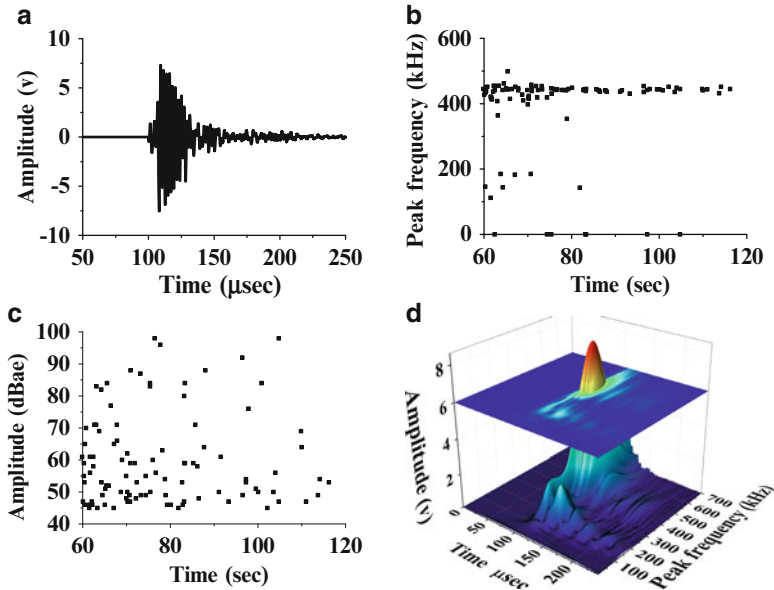


Fig. 6 AE results obtained by testing fiber bundle specimen; (a) AE waveform from fiber breakage, (b) PF, (c) amplitude, (d) wavelet analysis

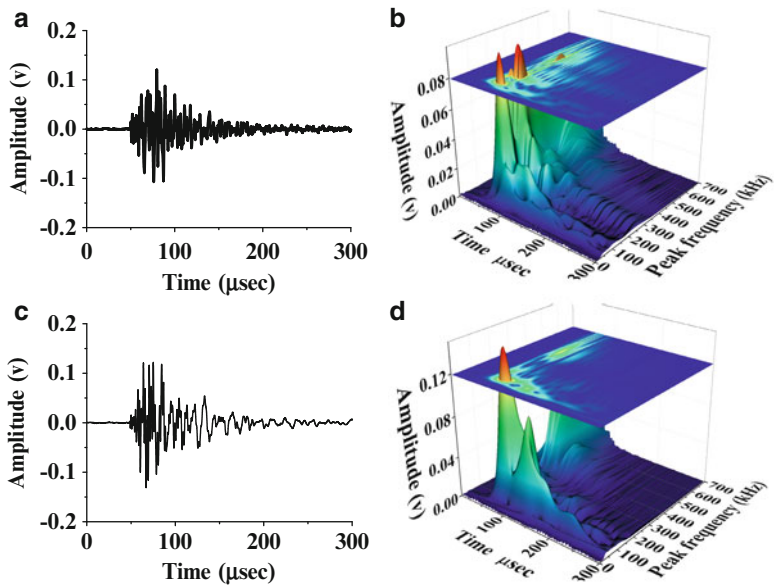


Fig. 7 AE results obtained by testing fiber-glass/matrix specimens; (a) a typical waveform of matrix cracking with fiber breakage, (b) wavelet analysis of the waveform at (a); (c) AE waveform possibly due to matrix cracking, (d) wavelet analysis of the waveform at (c)

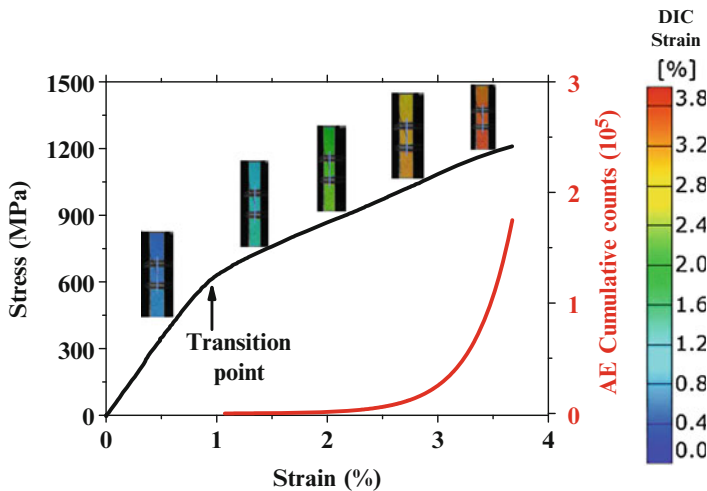


Fig. 8 Stress and AE cumulative counts versus strain as obtained in tensile test of Glare 1A

3.2 Glare 1A Quasi-Static Mechanical Behavior

Figure 8 illustrates the applied stress and cumulative AE counts versus strain obtained simultaneously by DIC (full field inserts) and the extensometer (X -axis values) for a representative uniaxial tensile test of Glare 1A. As shown, good agreement was found between the strain measurements provided by DIC (notice the DIC colorbar scale) and by the extensometer. The mechanical response of the FML is characterized by bilinear behavior, as also previously reported [18]. Significant AE activity initiated at the transition point between the elastic and plastic response (see arrow). The damage evolution during testing can be represented by both the exponential profile of the cumulative AE counts and the changes of the full field DIC strain maps.

To further quantify the fracture process of the tested Glare tensile specimen, AE data are displayed in Fig. 9a in terms of AE amplitude (Y -axis), PF (color range) and versus strain (obtained by the DIC method). Three peak frequencies are well emphasized by the used color range. The first one is around 50–150 kHz, the second between 200–300 kHz, and the highest one in the range between 400 and 450 kHz. To eliminate frequency range overlap and to identify the corresponding dominant failure mechanism and the sequence of their appearance, separated AE cumulative counts are shown in Fig. 9b. The lowest PF which was attributed to both plastic deformation (based on Fig. 5) and matrix cracking (based on Fig. 7) was extracted from AE signals recorded near the macroscopically observed yielding, while Fig. 9b shows that this group of AE signals continued to increase up to the final fracture. The second PF appeared mostly at and past the elastic plastic transition, while Fig. 9b shows that it saturates before the final fracture. The AE waveforms with these intermediates PFs are possibly correlated with interfacial micro-cracking

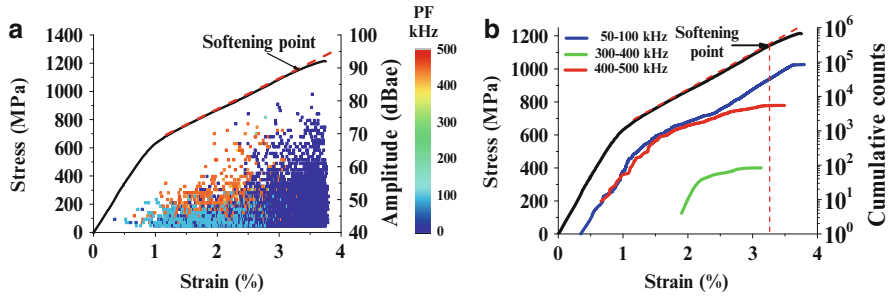


Fig. 9 (a) Stress and amplitude versus strain with peak frequency scale (b) stress and amplitude in cumulative manner at various peak frequencies

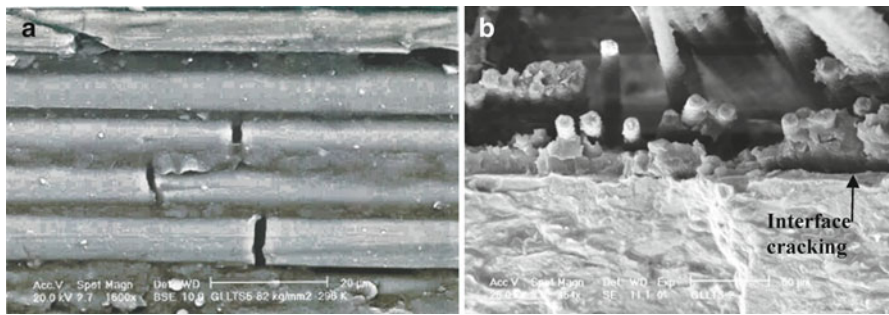


Fig. 10 Dominant fracture modes of Glare 1A tested in tension; (a) fiber breakage, (b) mixed mode fracture of Al-Alloy and S2-fiberglass layers

which appeared in later stages of deformation but ended near the softening zone shown by the arrows, and indicates the point past which the overall hardening rate appears to decrease. This quantitative description of the sequence of damage events based on AE information indicates that the contribution of the fibers, matrix, and interfaces reduces during the final stages of deformation which is dominated by Al-alloy micro-cracking as shown in Fig. 5.

Finally, Fig. 10 shows relevant microscopic images of the main fracture modes in Glare 1A tested in tension. Figure 10a demonstrates the fiber breakages mainly perpendicular to the loading axis. The fracture surface further revealed the ductile behavior of the Al-Alloy, de-bonding of the matrix–Al-layer interface, matrix cracking, and fractured fibers and the matrix–fiber interface.

3.3 Glare 1A Fatigue Behavior

Figure 11a. illustrates obtained results in terms of PFs as well as mechanical information (maximum strain per cycle, residual stiffness defined by the slope of the line defined by the line that connects the endpoints of each loop and energy

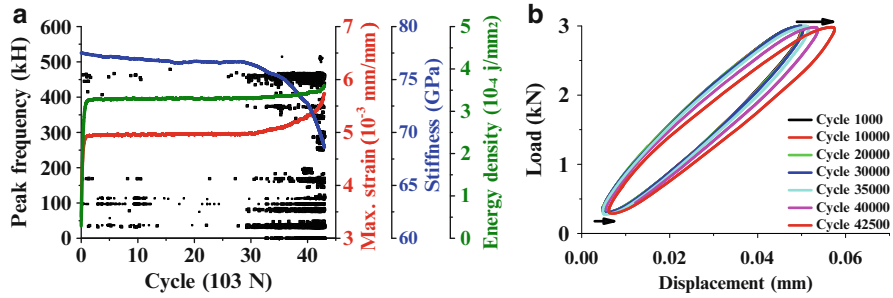


Fig. 11 Fatigue results of Glare 1A tested at cycling conditions of $\sigma_{\max} = 0.6\sigma_y$ with load ratio of 0.1; (a) PF and loop properties versus fatigue cycles, (b) the change of loop cycle during fatigue experiment

density defined as the enclosed area in each loop) extracted by the hysteretic cyclic behavior of a selected fatigue test with $\sigma_{\max} = 0.6\sigma_y$ and load ratio of 0.1. As the number of cycles increases the limits of the hysteresis loops and their enclosed area also increase (Fig. 11b). Up to $\sim 15,000$ cycles a moderate increase in the maximum strain and energy density occurs, accompanied by a same trend in the residual stiffness. In addition, both low and high PF values appear indicating matrix, matrix/interface, and fiber breakage together with plastic deformation mechanisms. From this point and up to $\sim 30,000$ cycles a relative silence in the AE activity is observed. This behavior may be attributed to crack arrest phenomena of the micro-cracks (mainly de-bonding delaminations at the interfaces) due to the laminate nature of this composite. Beyond this region dramatic changes are observed in the mechanical properties, namely, sudden decrease in the stiffness due to the massive cumulative damage accompanied by increasing maximum strain and energy density. These variations are further associated with a significant change in the AE activity due to development of several damage mechanisms. Fiber breakages occur just after the plateau region (PFs of around 450 kHz), followed by matrix micro-cracking (PFs about 50–100 kHz) and after that simultaneous activation of several damage mechanisms is possibly occurring: interface cracking with PFs of 100, 150 kHz, plastic deformation around 200 kHz, and micro-cracking at 400 kHz.

The mentioned damage mechanisms were also analyzed using FFT and relevant results displayed in terms of weighted peak frequency (Fig. 12a). The main peak frequencies are depicted and the dominant ones as defined by their intensity include fiber breakage and matrix cracking. Only for comparison to the quasi-static behavior, a wavelet analysis of an AE waveform possibly from fiber breakage is illustrated in Fig. 12b.

At the end of the fatigue loading the specimen was removed for damage characterization purposes and images were obtained by looking at the pre-polished thickness and the cross section normal to the applied load. Figure 13a demonstrates the characteristic breakage of the fibers which shows micro-cracking at different orientations. This damage is completely different from the one observed in quasi-static mode (see Fig. 10a) which appeared to consist of discrete cracks perpendicular to the applied loading direction. Figure 13b demonstrates interface cracking between the metal and

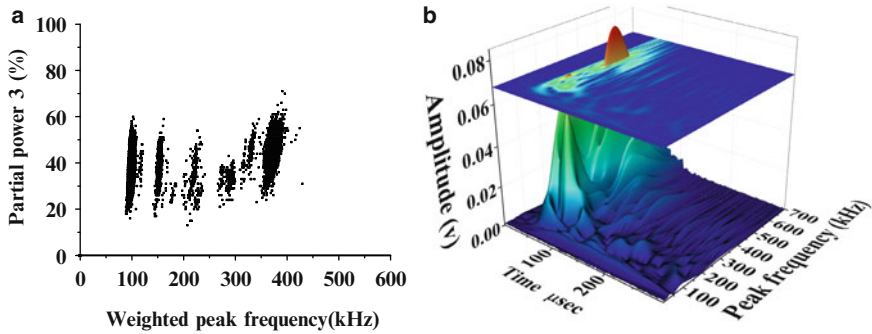


Fig. 12 (a) Weighted peak frequency results from partial power of AE signals at the end of fatigue test, (b) wavelet analysis of AE wave represent fiber breakage

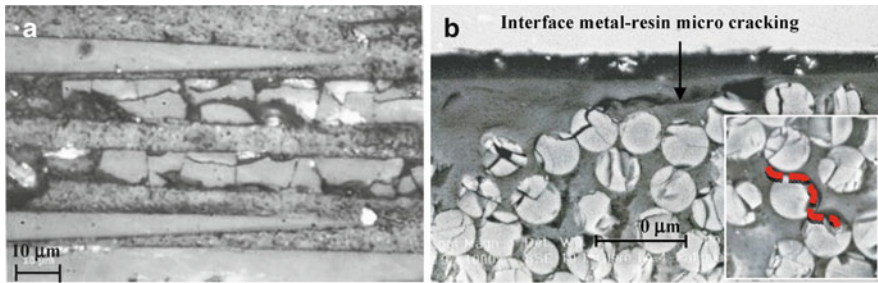


Fig. 13 Characteristic damage patterns during fatigue in two different views: (a) fiber fragmentation parallel to the loading direction, (b) fiber fragmentation at metal–resin interface, as well as fiber–matrix micro-cracking (see *curved dot line*) perpendicular to the loading direction

fiber/resin layer. As shown the micro-cracks occurred adjacent to interface as also observed in the quasi-static case (see Fig. 10b). The occurrence of cracks in this area may be attributed to the stress distribution resulting from the post-stretching at the final stage of the manufacturing process, namely, compressive stresses at the metal and tensile residual stresses at the fiber/resin layer.

3.4 Masonry Wall Damage Characterization

Figure 14a shows the loading history up until the end of the second cycle combined with the distribution of AE amplitude and the average strain that was measured by DIC at the bottom right area (see highlighted box in Fig. 14b). As one can notice, significant AE activity starts from the first loading cycle. This preferred site of damage is to be expected since this region transfers the horizontal applied load by the actuator to the wall foundation in a cyclic mode. As a consequence massive deformation and cracking occurs as the load changes from tensile to compression mode.

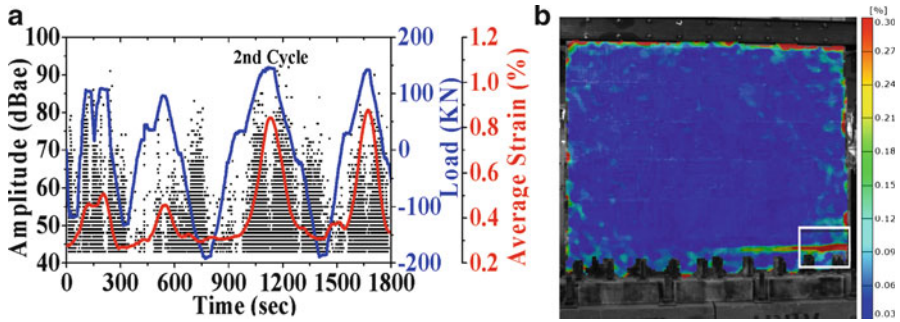


Fig. 14 Continuous monitoring results up to the second cycle of the loaded masonry wall: (a) AE activity combined with load and DIC average strain as measured in the square area shown on the bottom right corner, (b) full field DIC principal strain at the peak load of the second cycle

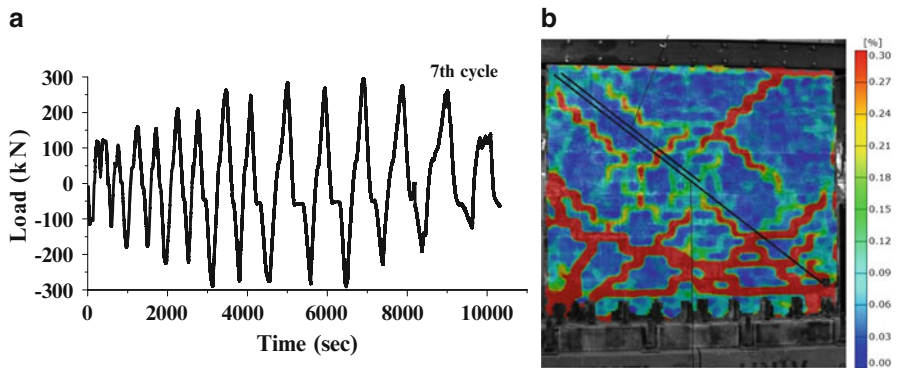


Fig. 15 Final stage of the loaded wall; (a) the load history up to fracture, (b) DIC strain mapping indicating extensive macro-cracks network

At the first cycle, a good correlation exists between AE activity and DIC measurements. High AE amplitude values were detected accompanied by high local deformation indicated by a pronounced damage development at this area. Increasing the load by 50 %, increases significantly the localized measured strain by DIC. In addition, the AE amplitude increases from 80 dBae to more than 95 dBae (at the peak load) which can be mostly attributed to interface cracking as shown by the DIC pictures. Post loading visual inspection assessed those results and revealed a micro-crack in the form of hairline cracks along the mortar. It is also worth mentioning that both AE and DIC provided early signs of cracking far before visual inspection could detect those hairline cracks. This mutual correlation between AE and DIC has significant importance in terms of validating real AE signals and filtering noise due to friction, vibration, hydraulic flow, and mechanical impact, among other reasons.

Finally, Fig. 15 displays the last stage of the loaded wall which manifests catastrophic damage. Figure 15a shows the loading history of the entire test. As it

can be noticed the seventh load cycle shows a decrease in the load amplitude due to significant accumulated damage. The latter is being well reflected by the DIC measurements, revealing an extended a micro-crack network (Fig. 15b).

4 Discussion

The present study accentuates the great potential of using a variety of advanced techniques together with common ones in order to understand in a comprehensive way fundamental aspects related to plastic deformation, micro-cracking, evolution of damage and its profile quantified in both monotonic and cyclic loading conditions. With respect to structural durability, the integration of both techniques illustrates in real time the damage progression and highlights the preferential sites of intensified damage.

The comprehensive work on the Glare-1A with its complicated structure emphasizes the potential of the combination of the AE and DIC methods to reveal its deformation and fracture behavior. The mechanical response of this hybrid composite is characterized by bilinear behavior with a secondary low modulus (E_p) at the plastic regime as compared to the higher one at the elastic region. The observed E_p is a consequence of the competitive activation of several damage mechanisms. The evolving plasticity of the Al-alloy contributes to the overall strain hardening (similar to monolithic Al-Alloy) whereas the other damage mechanisms of the resin/fiber layers, the fiber breakages, and the matrix cracks contribute to softening. This competition appears to end (see the softening point in Fig. 9b) when the damage in the resin/fiber layer is substantial as compared to strain hardening contributions, which leads to localized “necking” followed by a decrease in the stress and causes the final fracture. This argument is based on the fracture sequences revealed by the NDT measurements in this paper which visually show the localized strain regions in the Al-Alloy.

Damage evolution can be represented by the exponential growth of the cumulative AE energy. In addition, significant AE activity initiates at a characteristic threshold strain. From practical/engineering point of view, it is important to know this value in cases where no damage can be tolerated for proper functioning (fail-safe approach). The exponential profile of the damage modeled in terms of AE information is very similar to a micro-mechanical damage model suggested by Talreja [19], for inter-laminar cracking in composite laminates such as the tested FML. Talreja proposed the use of a damage tensor defined as:

$$D_{ij} = \frac{k \cdot t_c^t}{s \cdot t \cdot \cos \theta} n_i \cdot n_j \quad (1)$$

where t is the thickness of the specimen, t_c is the ply thickness, s the crack spacing, θ the angle between the fiber direction and the transverse direction, and $n = (\cos h, \sin h, 0)$. By using a thermodynamic framework for the description of the

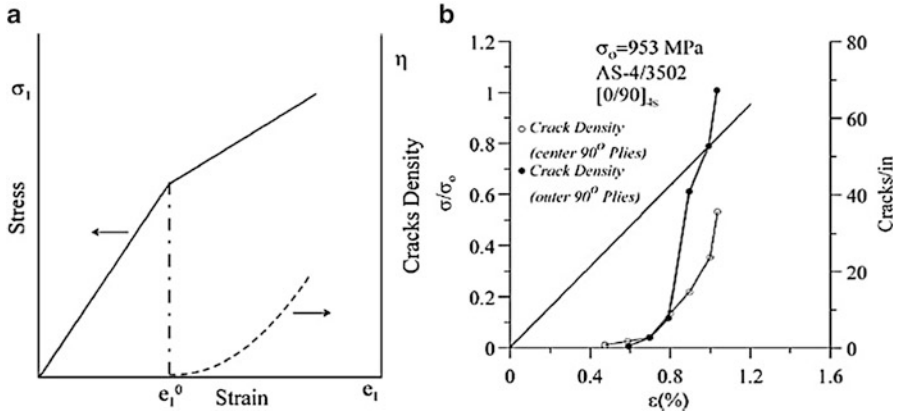


Fig. 16 (a) A bilinear stress–strain behavior with associated transverse crack density and (b) experimental stress–strain curve and associated transverse crack density of a graphite–epoxy (0, 90) [20]

material response, Talreja further determined D_1 for a bilinear stress–strain curve in the following form:

$$\log \frac{D_1}{D_1^0} = \frac{E_t}{\eta} [d_4(e_1 - e_0^1)] + [A\{e_0^2 - (e_0^1)^2\} + B\{e_1^3 - (e_0^1)^3\}] \quad (2)$$

where D_1^0 is the initial damage (initial crack density) that begins to grow at threshold strain e_1^0 and E_t the tangent modulus beyond the initiation of damage growth. Combining Eq. (1) for the non-zero component of damage tensor and Eq. (2) with $g = 1 \text{ s}^{-1}$, gives the crack density as an exponential function of strain, as shown schematically in Fig. 16a by the dashed curve. The predicted profile is in agreement with experimental results such as the ones obtained by Kistner et al. [21] in graphite–epoxy composites shown in Fig. 16b. The exponential behavior of the crack density vs. strain was also viewed in NCF cross-ply laminates up to the transition point where damage coalescence is operating [20]. These observations strengthen the argument that AE is a powerful tool in damage characterization especially when used in combination with other complementary NDT methods, such as the DIC presented in this paper.

The field work on a reinforced masonry wall contributed decisively in determining the optimum reinforcing steel beam pattern (consisting mainly by reinforced beams in appropriate distance from each other, and all perpendicular to the applied load) to withstand earthquake-type loads. The findings of both NDT techniques used in this paper are relatively straightforward. In other words the current results emphasize the potential of these characterization tools for appropriate engineering decisions. Furthermore, it is well known that shear forces are responsible for major damage modes during applied loading. When these forces cause a major damage, a

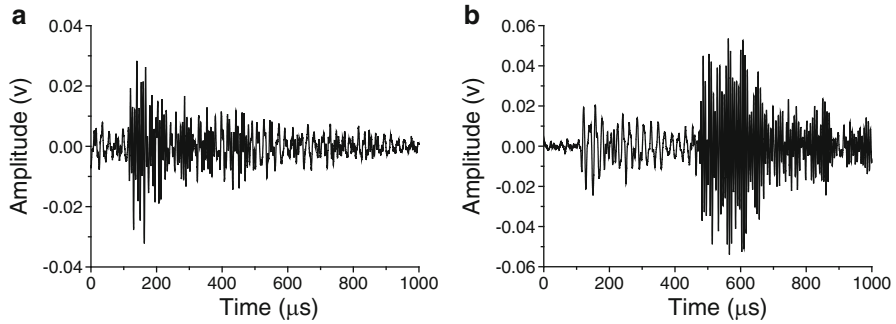


Fig. 17 Typical AE waves that were recorded during different stages of loading; (a) Mode I early stages, (b) mode II at cycle 2 and beyond

shear wave is emitted due to pertinent movement in the damaged area. The AE wave typically composed of a longitude and transverse wave, when the shear mode is dominant shows a relatively late arrival of its peak amplitude [22]. Therefore by analyzing the shear component of recorded AE waves one can predict the damage severity of a structure [23]. On these experiments a good correlation between AE and DIC achieved using shear wave analysis. In this context, Fig. 17 illustrates typical longitudinal and shear waves that were analyzed during different stage in the experiment.

5 Conclusions

Application and research results from integrating of DIC and AE are presented in this article. Combined data can assist the characterization of the mechanical behavior of fiber metal laminates. As for the wall, the AE-DIC combined data can serve to form an important basis for engineering considerations that can ensure structural performance in extreme conditions. The following conclusions can be drawn from the recent work:

1. The bilinear mechanical behavior of Glare 1A is a consequence of the competitive activation of several damage mechanisms, including plastic deformation and micro-cracking coalescence at the Al-Alloy, as well as fiber breakage and interfacial de-bonding at metal/resin layer in addition to fiber/matrix and matrix cracking. The softening behavior occurs as the balance of these mechanisms is interrupted.
2. The obtained AE data highlight the operated damage mechanisms and their sequence appearance in terms of characteristics PF and damage evolution with exponential profile. This AE activity follows the same trend with suggested micro-mechanical models for damage development in terms of crack density for laminated composites.

3. The AE-DIC data reveal critical damage areas of the loaded wall as a function of applied loading, providing in this way early signs of deterioration that can be implemented in structural health monitoring applications.

Acknowledgment The authors wish to thank Prof. Ahmad Hamid and Prof. Frank Moon from the Civil engineering Dept. at Drexel University, for assistance in conducting the tests on the masonry wall.

References

1. R.K. Miller, P. McIntire, *Nondestructive Testing Handbook, Vol 6: Acoustic Emission Testing* (American Society for Nondestructive Testing, Columbus, OH, 2005), p. 447
2. M. Sutton et al., Application of an optimized digital correlation method to planar deformation analysis. *Image. Vision. Comput.* **4**(3), 143–150 (1986)
3. T. Chu, W. Ranson, M. Sutton, Applications of digital-image-correlation techniques to experimental mechanics. *Exp. Mech.* **25**(3), 232–244 (1985)
4. B. Pan et al., Two-dimensional digital image correlation for in-plane displacement and strain measurement: a review. *Meas. Sci. Technol.* **20**(6), 062001 (2009)
5. M.A. Sutton, J.J. Orteu, H.W. Schreier, *Image Correlation for Shape, Motion and Deformation Measurements: Basic Concepts, Theory and Applications* (Springer, New York, 2009)
6. J. Cuadra et al., Damage quantification in polymer composites using a hybrid NDT approach. *Compos. Sci. Technol.* **83**, 11–21 (2013)
7. E. Schwartz et al., *The Use of Digital Image Correlation for Non-destructive and Multi-scale Damage Quantification. In SPIE Smart Structures and Materials + Nondestructive Evaluation and Health Monitoring* (International Society for Optics and Photonics, Bellingham, WA, 2013)
8. P.A. Vanniamparambil et al., An integrated structural health monitoring approach for crack growth monitoring. *J. Intel. Mat. Syst. Struct.* **23**(14), 1563–1573 (2012)
9. T. Beumler, Flying Glare. A contribution to aircraft certification issues on strength properties in non-damaged and fatigue damaged GLARE® structures. Dissertation, Faculty of Aerospace Engineering, Technical University Delft, 2004
10. A. Vlot, *Glare: History of the development of a New Aircraft Material* (Kluwer, New York, 2001)
11. C. Vermeeren et al., Glare design aspects and philosophies. *Appl. Compos. Mater.* **10**(4–5), 257–276 (2003)
12. G. Wu, J.M. Yang, The mechanical behavior of GLARE laminates for aircraft structures. *JOM* **57**(1), 72–79 (2005)
13. ASTM E976, *Standard Guide for Determining the Reproducibility of Acoustic Emission Sensor Response* (ASTM, West Conshohocken, PA, 2005)
14. A. Anastassopoulos, T. Philippidis, Clustering methodology for the evaluation of acoustic emission from composites. *J. Acoustic. Emission.* **13**(1–2), 11–22 (1995)
15. M. Sause et al., Quantification of failure mechanisms in mode-I loading of fiber reinforced plastics utilizing acoustic emission analysis. *Compos. Sci. Technol.* **72**(2), 167–174 (2012)
16. M. Kempf, O. Skrabala, V. Altstädt, Acoustic emission analysis for characterisation of damage mechanisms in fibre reinforced thermosetting polyurethane and epoxy. *Compos. B Eng.* **54**, 289–299 (2013)
17. P.A. Vanniamparambil, R. Carmi, F. Khan, I. Bartoli, A. Kotsos, Novel optico-acoustic sensing system for cross-validated structural health monitoring, in *ICOSSAR 2013 – the 11th International Conference on Structural Safety & Reliability* (Columbia University, New York, NY, 2013)

18. A. Bussiba et al., Damage evolution and fracture events sequence in various composites by acoustic emission technique. *Compos. Sci. Technol.* **68**(5), 1144–1155 (2008)
19. R. Talreja, Damage development in composites: mechanisms and modelling. *J. Strain Anal. Eng. Des.* **24**(4), 215–222 (1989)
20. F. Edgren et al., Formation of damage and its effects on non-crimp fabric reinforced composites loaded in tension. *Compos. Sci. Technol.* **64**(5), 675–692 (2004)
21. M.D. Kistner, J.M. Whitney, C.E. Browning, First-ply failure of graphite/epoxy laminates. *Recent Adv. Compos. US Jpn ASTM STP* **864**, 44–61 (1985)
22. K. Ohno, M. Ohtsu, Crack classification in concrete based on acoustic emission. *Construct. Build Mater.* **24**(12), 2339–2346 (2010)
23. A. Farhidzadeh, S. Salamone, P. Singla, A probabilistic approach for damage identification and crack mode classification in reinforced concrete structures. *J. Intel. Mat. Syst. Struct.* **24**(14), 1722–1735 (2013)